

# Microstructure and Cyclic Deformation Behavior of a Friction-Stir-Welded 7075 Al Alloy

A.H. FENG, D.L. CHEN, and Z.Y. MA

Microstructural changes and cyclic deformation characteristics of friction-stir-welded 7075 Al alloy were evaluated. Friction stir welding (FSW) resulted in significant grain refinement and dissolution of  $\eta'$  ( $\text{Mg}(\text{Zn},\text{Al},\text{Cu})_2$ ) precipitates in the nugget zone (NZ), but  $\text{Mg}_3\text{Cr}_2\text{Al}_{18}$  dispersoids remained nearly unchanged. In the thermomechanically affected zone (TMAZ), a high density of dislocations was observed and some dislocations were pinned, exhibiting a characteristic Orowan mechanism of dislocation bowing. Two low-hardness zones (LHZs) between the TMAZ and the heat-affected zone (HAZ) were observed, with the width decreasing with increasing welding speed. Cyclic hardening and fatigue life increased with increasing welding speed from 100 to 400 mm/min, but were only weakly dependent on the rotational rate between 800 and 1200 rpm. The cyclic hardening of the friction-stir-welded joints exhibiting a two-stage character was significantly stronger than that of the base metal (BM) and the energy dissipated per cycle decreased with decreasing strain amplitude and increasing number of cycles. Fatigue failure occurred in the LHZs at a lower welding speed and in the NZ at a higher welding speed. Fatigue cracks initiated from the specimen surface or near-surface defects in the friction-stir-welded joints, and the initiation site exhibited characteristic intergranular cracking. Crack propagation was characterized by typical fatigue striations along with secondary cracks.

DOI: 10.1007/s11661-009-0152-3

© The Minerals, Metals & Materials Society and ASM International 2010

## I. INTRODUCTION

THE 7xxx-series aluminum alloys are precipitation-hardened Al-Zn-Mg-(Cu) alloys that have been used extensively in the aircraft structural components, mobile equipment, and other highly stressed applications.<sup>[1]</sup> Zinc and magnesium are the main alloying elements. The undesirable iron and silicon impurities are present in the form of coarse constituent particles, *i.e.*,  $\text{Al}_7\text{Cu}_2\text{Fe}$ ,  $\text{Al}_2\text{CuMg}$ , and  $\text{Mg}_2\text{Si}$ .<sup>[2,3]</sup> Zirconium or chromium is added to retard recrystallization and control grain size.<sup>[4]</sup> Most 7xxx-series aluminum alloys can be categorized in two groups, depending on the type of grain structure and controlling element: Zr-containing alloys ( $\text{Al}_3\text{Zr}$ ) and Cr-containing alloys ( $\text{Al}_7\text{Cr}$ ).<sup>[5]</sup>

Friction stir welding (FSW), invented at The Welding Institute (Cambridge, United Kingdom) in 1991, is an environmentally friendly, energy-effective, and versatile solid-state joining technique capable of welding light-weight materials, *i.e.*, 7xxx-series aluminum alloys, which are relatively difficult to weld using conventional fusion welding techniques.<sup>[6,7]</sup> It is thus considered to be the most significant development in materials joining in the past two decades. It is therefore essential to identify

the relationships among joining parameters, microstructures, and mechanical properties.

Extensive studies of the FSW/friction stir processing of 7xxx-series aluminum alloys have been reported, including studies of the precipitation sequence,<sup>[8–10]</sup> recrystallization mechanisms,<sup>[4,11,12]</sup> superplasticity,<sup>[13,14]</sup> material flow,<sup>[15]</sup> residual stresses,<sup>[16]</sup> and mechanical properties.<sup>[17–26]</sup> While the FSW of aluminum alloys has engendered considerable scientific and technological interest, material property data are still limited, especially on fatigue properties that directly limit the widespread applications of the FSW process.<sup>[7,18–26]</sup>

The 7xxx-series aluminum alloys exhibit very high strength but also poor ductility and high notch sensitivity.<sup>[27]</sup> The fatigue of the commercial 7075Al-T6 alloy has received considerable attention.<sup>[28]</sup> The FSW offers high joint quality and good fatigue performance.<sup>[22]</sup> From an engineering design perspective, the fatigue properties of the friction-stir-welded aluminum alloys are of particular importance. This has led to increasing research interest in evaluating the fatigue resistance of the friction-stir-welded joints, including the stress number of cycles to failure behavior<sup>[20,22,25,26]</sup> and fatigue crack propagation behavior.<sup>[7,18,19,21]</sup> Previous studies indicated the following results.<sup>[7]</sup> First, the fatigue strength of the friction-stir-welded joints at  $10^7$  cycles was lower than that of the base metal (BM).<sup>[24]</sup> Second, the surface quality of the friction-stir-welded joints had a significant effect on the fatigue strength of the joints. Third, the effect of FSW parameters on fatigue strength was complicated and no consistent trend was obtained so far. In particular, studies of the low-cycle-fatigue (LCF) behavior of friction-stir-welded aluminum alloys have been limited;<sup>[29–31]</sup> these are indeed

A.H. FENG, Postdoctoral Fellow, and D.L. CHEN, Professor and Ryerson Research Chair, are with the Department of Mechanical and Industrial Engineering, Ryerson University, Toronto, ON M5B 2K3, Canada. Contact e-mail: dchen@ryerson.ca Z.Y. MA, Professor, is with the Shenyang National Laboratory for Materials Science, Institute of Metal Research, Chinese Academy of Sciences, Shenyang 110016, P.R. China.

Manuscript submitted July 8, 2009.

Article published online January 22, 2010

required by the automobile manufacturer to estimate the lifetime of components. The LCF of friction-stir-welded Al-Mg alloys tested in air and 3.5 pct NaCl solution by Czechowski<sup>[29]</sup> and of friction-stir-welded AA6061/Al<sub>2</sub>O<sub>3</sub>p and AA7005/Al<sub>2</sub>O<sub>3</sub>p joints by Ceschini *et al.*<sup>[30,31]</sup> has recently been reported. To date, no LCF information about the friction-stir-welded 7xxx-series aluminum alloy is available in the literature. The objectives of the present study were, therefore, as follows: to (1) study the LCF behavior and undertake detailed microstructural examinations of the friction-stir-welded 7075Al-T651 alloy, (2) identify the effect of FSW parameters on the microstructural evolution and LCF properties of the welds, and (3) evaluate the cyclic deformation characteristics and fatigue life under varying strain amplitudes.

## II. MATERIAL AND EXPERIMENTAL PROCEDURE

Commercial 7075Al-T651 rolled plates 6.35-mm thick (400-mm long and 80-mm wide), with a composition of 5.6Zn-2.5Mg-0.5Fe-0.16Cu-0.23Cr-0.3Mn-0.2Ti (wt pct), were friction stir welded along the rolling direction using an FSW machine (China FSW Center, Beijing FSW Technology Ltd., Beijing, China). A steel tool with a shoulder 20 mm in diameter and a cylindrical threaded pin 8 mm in diameter was used. The tool rotational rates were selected to be from 800 to 1200 rpm, and the welding speeds were from 100 to 400 mm/min. The friction-stir-welded work piece is schematically shown in Figure 1.

The specimens for microstructural examinations were cross sectioned perpendicular to the FSW direction. Microstructural characterization and analysis were carried out using optical microscopy (OM) and scanning

electron microscopy (SEM) (JEOL\* JSM-6380LV)

\*JEOL is a trademark of Japan Electron Optics Ltd., Tokyo.

coupled with energy-dispersive X-ray spectroscopy (EDS), X-ray diffractometry (XRD) (D/max 2500 PC, Rigaku Corporation, Tokyo, Japan), differential scanning calorimetry (DSC) (Q1000V9.4 Build287, TA Instruments, New Castle, DE), and transmission electron microscopy (TEM) (FEI TECNAIG2, FEI Company, Hillsboro, OR). Typically, approximately 15 mg of the DSC sample in the form of a 4-mm-diameter disk was heated at 10 °C min<sup>-1</sup> (10 K min<sup>-1</sup>) from 30 °C (303 K) to 520 °C (793 K) under a flowing argon atmosphere with a pure alumina crucible. The specimens for OM and SEM were prepared by mechanical grinding, polishing, and etching using Keller's reagent. Grain sizes were estimated by the linear intercept method. The TEM foils, 3 mm in diameter, were prepared by twin-jet electropolishing using a solution of 70 pct methanol and 30 pct nitric acid at -35 °C (238 K) and 19 V.

Vickers microhardness distribution maps were measured on the cross section perpendicular to the welding direction using a computerized Buehler hardness tester (Buehler, Lake Bluff, IL) under a load of 300 g for 15 seconds. A total of seven test lines were measured through the cross section at an interval of 0.5 mm, with a total of 567 indentations, as schematically shown in Figure 1.

Subsized fatigue specimens following ASTM E8 standards, with a reduced parallel section 32 × 6 × 5.6 mm in size, were machined perpendicular to the FSW direction, as shown in Figure 1. The friction-stir-welded joint fringes on the top surface were first removed by 0.4 mm, and then the bottom surface 0.35 mm in thickness was removed while keeping the

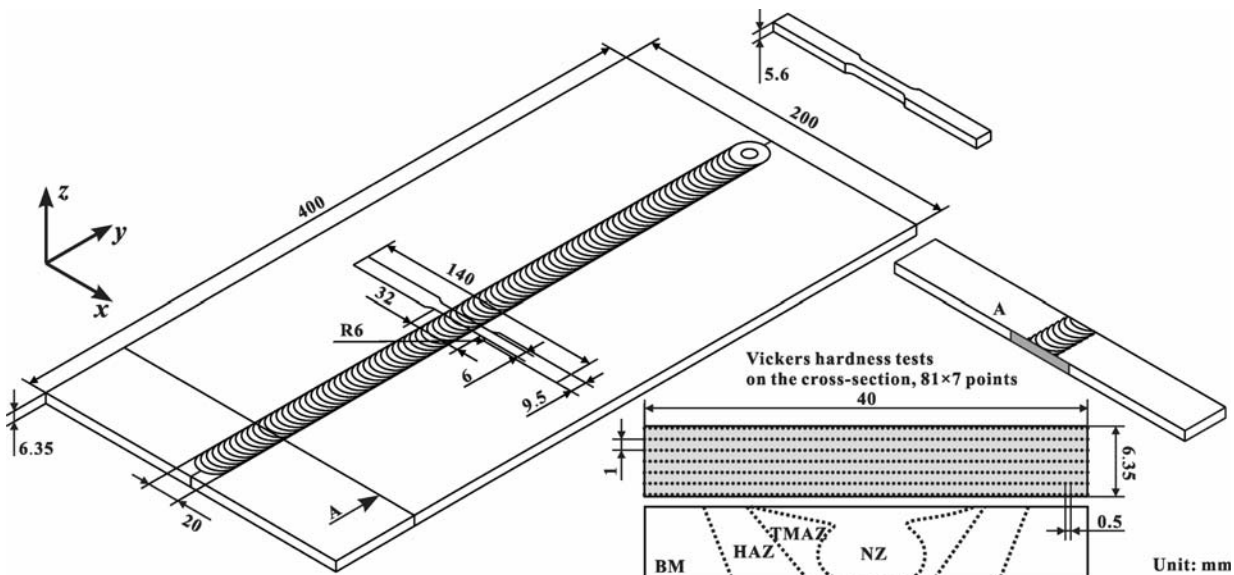


Fig. 1—Schematic illustration of friction-stir-welded 7075Al-T651 joints for fatigue specimen machining and microhardness tests, together with an indication of various zones across the weld (BM, HAZ, TMAZ, and NZ).

final specimen thickness to 5.6 mm. The fatigue specimens, prepared *via* a computer numerical controlled machine, were ground with SiC papers up to grit #600 to get rid of the machining marks and to achieve a smooth surface. Total-strain-controlled, push-pull-type LCF tests were conducted using a computerized Instron fatigue testing system (Instron 8801, Instron Corporation, Norwood, MA). In the fatigue testing, a triangular waveform with a strain ratio of  $R = -1$  was applied at a constant strain rate of  $1 \times 10^{-2} \text{ s}^{-1}$ . The strain-controlled testing at low total strain amplitudes was operated until 10,000 cycles, after which it was changed to a load-control test at a frequency of 50 Hz. Total strain amplitudes of 0.2 to 1.0 pct were selected in the LCF tests, where at least two specimens were tested at each level of the strain amplitudes. After the fatigue tests, the crack initiation sites and propagation mechanisms were examined *via* SEM.

### III. RESULTS

#### A. Microstructure

The XRD pattern of the 7075Al-T651 alloy revealed the presence of Al,  $\text{Al}_7\text{Cu}_2\text{Fe}$ ,  $\text{MgZn}_2$ , and  $\text{Mg}_3\text{Cr}_2\text{Al}_{18}$  phase (Figure 2(a)). The heat flow of the 7075Al-T651 alloy, measured as a function of the temperature, is shown in Figure 2(b). The endothermic peak A at approximately 188 °C (461 K) observed in the DSC curve indicated the dissolution of  $\eta'$  ( $\text{Mg}(\text{Zn}, \text{Al}, \text{Cu})_2$ ).<sup>[32]</sup>

The 7075Al-T651 alloy was characterized by the large, elongated, pancake-shaped grains several hundred micrometers long in the transverse direction and approximately 20- $\mu\text{m}$  wide in the normal (or short transverse) direction resulting from the rolling process (Figure 3(a)). Strings of elongated inclusion particles 2 to 5  $\mu\text{m}$  in size could also be seen. The white inclusion particles were determined to be  $\text{Al}_7\text{Cu}_2\text{Fe}$  by EDS analyses, composed of approximately 47Al, 12Fe, and 41Cu (wt pct) (Figure 3(b)). Figure 3(c) shows the subgrains' structures. Platelet  $\eta'$ , ranging from approximately

1.2- to 2.5-nm thick and 4.5- to 6-nm long, was observed in Figure 3(d).

Figure 4 shows typical cross-sectional macrostructures of the friction-stir-welded 7075Al-T651 joints obtained in different welding conditions. Under the selected welding parameters, no welding defects were detected in the friction-stir-welded joints. Three zones, *i.e.*, a nugget zone (NZ), a thermomechanically affected zone (TMAZ), and a heat-affected zone (HAZ), were discernible. The shapes of the NZ were apparently parameter dependent. The interface between the NZ and TMAZ in the advancing side (AS) was more distinctly visible than that in the retreating side (RS).

The microstructure of the NZ was characterized by fine and equiaxed grains with average grain sizes from 4.6 to 6.7  $\mu\text{m}$ , respectively (Figure 5). The average grain size decreased with an increasing welding speed from 100 to 400 mm/min (Figures 5(a) through (c)). However, the average grain size changed little with an increasing rotational rate from 800 to 1000 rpm while keeping the welding speed constant (Figures 5(c) and (d)).

After FSW, the NZ was characterized by a fine and equiaxed recrystallized grain structure (Figure 6(a)). In contrast to the BM, the dislocation density in the NZ was quite low. The scanning transmission electron microscopy (STEM) image indicated that a considerable amount of dispersoids were randomly distributed, which were determined to be chromium-rich dispersion  $E$  phase ( $\text{Mg}_3\text{Cr}_2\text{Al}_{18}$ ) (Figures 6(b) and (c)), as reported in Reference 28, as well. No other fine precipitates were observed *via* TEM examinations.

Severe bending of grains was observed in the TMAZ region (Figure 7(a)). Most grains in the TMAZ contained a high dislocation density with a network subgrain structure (Figure 7(b)). The coarsened precipitates were observed within the grain or at the subgrain boundaries (Figures 7(b) and (c)). Dislocations were pinned by  $\text{Mg}_3\text{Cr}_2\text{Al}_{18}$  dispersoids (Figure 7(d)). Individual dislocations extended between particles, but no tangles occurred, exhibiting a characteristic Orowan mechanism of dislocation bowing.

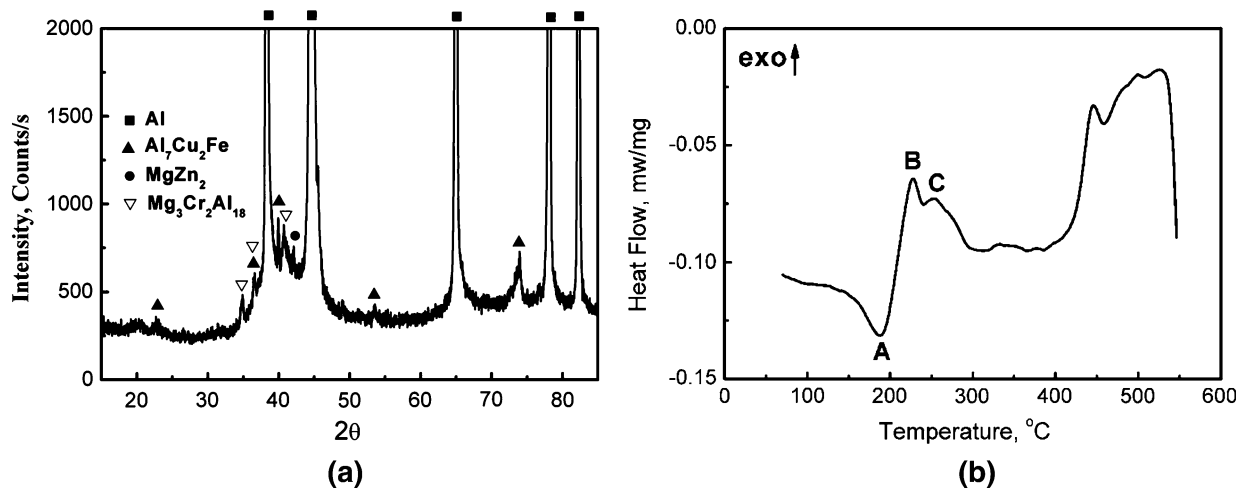


Fig. 2—(a) XRD pattern and (b) DSC curve of 7075Al-T651 alloy.

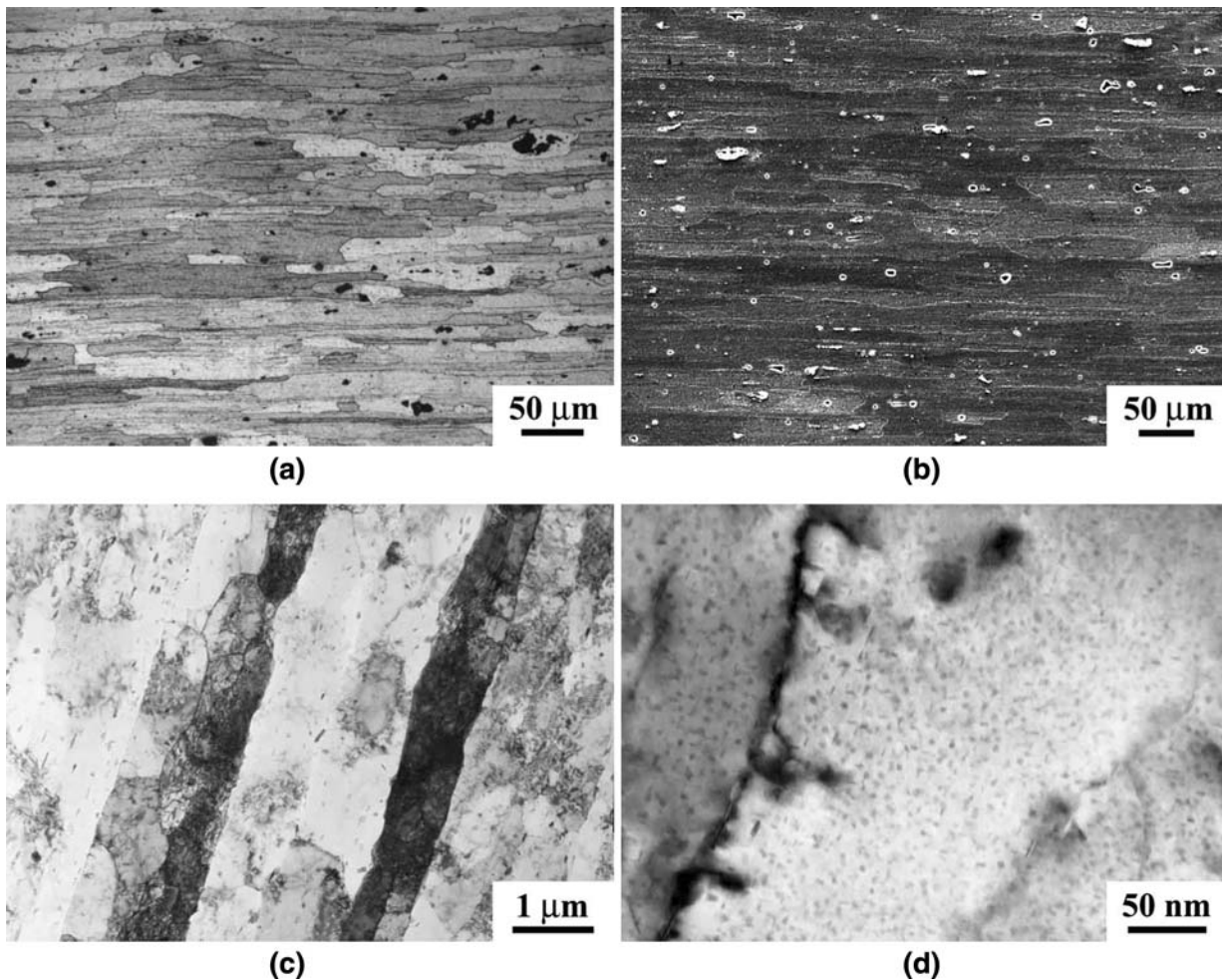


Fig. 3—Microstructures of 7075Al-T651 alloy: (a) OM image showing elongated pancake grains, (b) SEM micrograph, (c) TEM image showing subgrain structure, and (d) higher-magnification TEM image showing the tiny and uniformly distributed precipitates.

### B. Microhardness

Figure 8 shows the microhardness contour maps for the friction-stir-welded 7075Al-T651 joints with different FSW parameters. Two low-hardness zones (LHZs), located between the TMAZ and HAZ, were obviously observed. The width of the LHZs increased with decreasing welding speed from 400 to 100 mm/min. The slight asymmetry of the weld was noticeable between the AS and RS.

### C. Cyclic Deformation Characteristics

Figure 9 shows the stress amplitude and plastic strain amplitude vs the number of cycles at a given rotational rate of 800 rpm and at different welding speeds. Three important observations can be summarized (Figure 9(a)). First, the stress amplitude increased with increasing strain amplitude. Second, the stress amplitudes of the friction-stir-welded joints were lower than that of the BM. Third, the cyclic hardening of the friction-stir-welded joints, which increased with increasing welding speed, was much stronger than that of the

BM. As the total strain amplitude increased, the value of the plastic strain amplitude also increased and the fatigue life of the samples decreased (Figure 9(b)).

Figure 10 shows the stress amplitude and plastic strain amplitude vs the number of cycles at a given welding speed of 400 mm/min and different rotational rates. The results indicated that the cyclic hardening of the friction-stir-welded joints was nearly independent of the rotational rates at a given strain amplitude.

### D. Fractography

Figure 11 shows some typical fatigue fracture surfaces of the friction-stir-welded samples (800 rpm and 100 mm/min), which failed along the LHZs between the TMAZ and HAZ with an angle of ~45 degrees to the tensile axis on the AS (Figure 11(a)). It is seen that the fatigue crack initiated from the specimen surface, as denoted by the dashed semicircle in Figure 11(b). Crack propagation was characterized by the characteristic striation-formation mechanism (Figures 11(c) through (e)). The inclusion particles were lined up due to the rolling process (Figure 11(d)). Some white particles

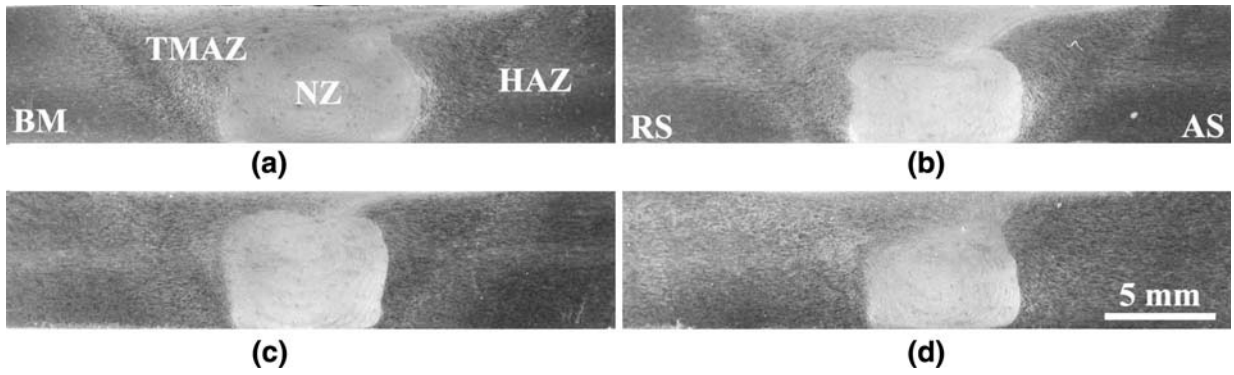


Fig. 4—Cross-sectional macrostructures of friction-stir-welded 7075Al-T651 joints: (a) 800 rpm and 100 mm/min, (b) 800 rpm and 200 mm/min, (c) 800 rpm and 400 mm/min, and (d) 1000 rpm and 400 mm/min.

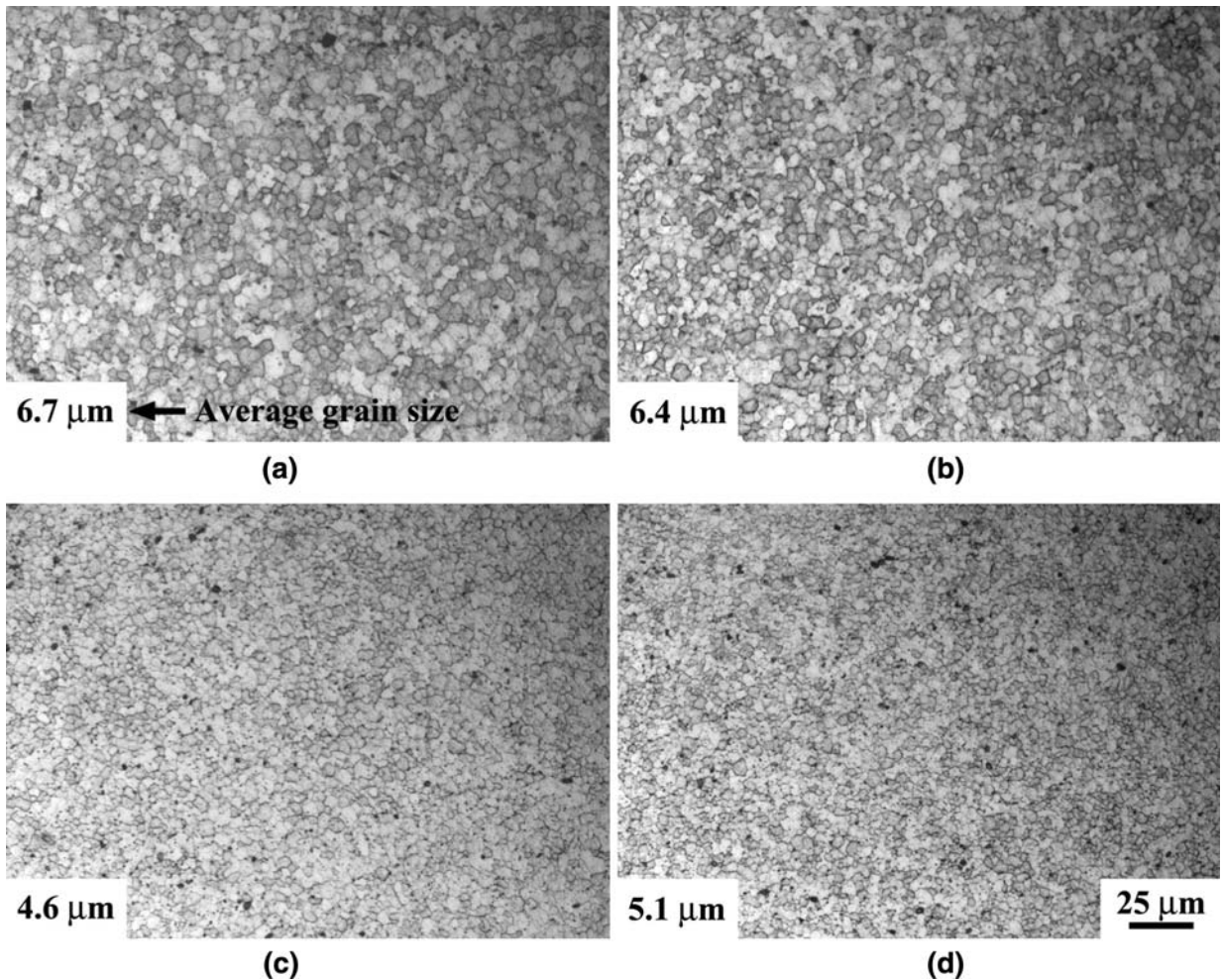


Fig. 5—Cross-sectional microstructures in NZ of friction-stir-welded 7075Al-T651 joints: (a) 800 rpm and 100 mm/min, (b) 800 rpm and 200 mm/min, (c) 800 rpm and 400 mm/min, and (d) 1000 rpm and 400 mm/min.

appeared on the fracture surface of the friction-stir-welded sample, which could be better seen from the backscattered electron image (BEI) (Figures 11(d) and (e)). The EDS analyses revealed that the white particles contained a large amount of iron and copper (67Al, 10Fe, and 23Cu (wt pct)) (Figure 11(e)).

Figure 12 shows some typical fatigue fracture surfaces of the friction-stir-welded samples (800 rpm and 400 mm/min), in which a macroscopic image of a failed LCF specimen is illustrated in Figure 12(a). The fracture surface displayed multiple sites of fatigue crack initiation, but all from the specimen surface, as indicated by

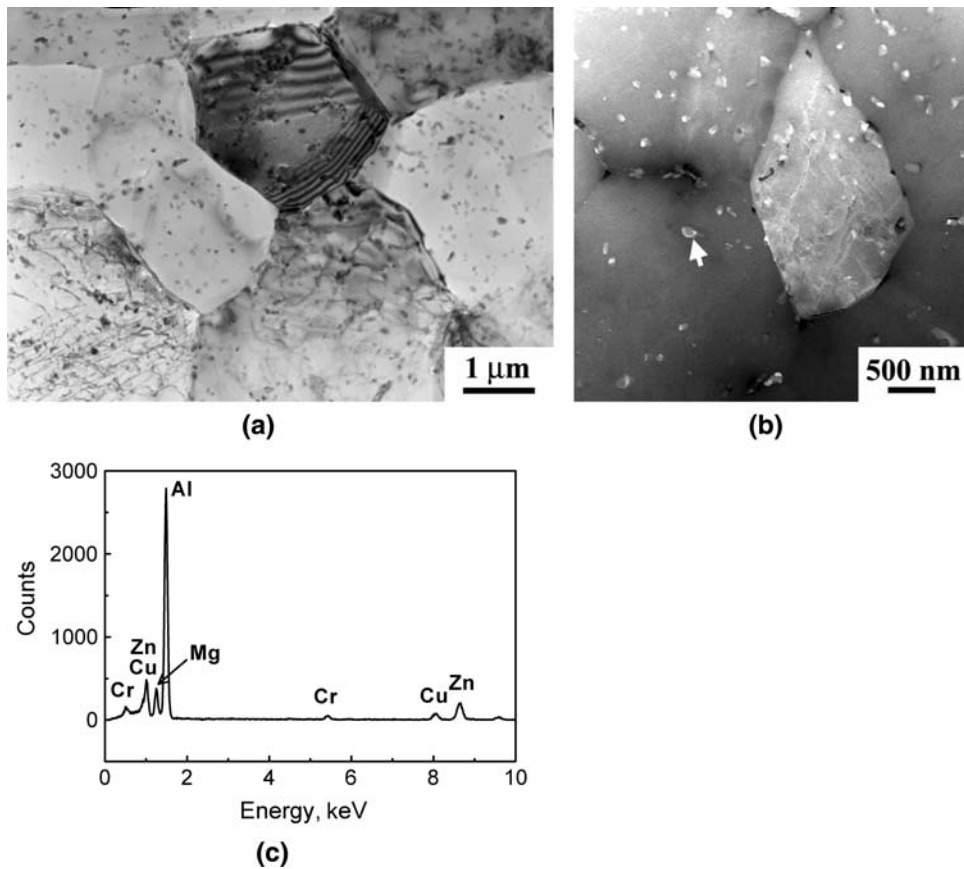


Fig. 6—Microstructure of NZ in friction-stir-welded 7075Al-T651 alloy (800 rpm and 400 mm/min): (a) TEM image, (b) STEM image, and (c) EDS spectrum.

the three dashed semicircles in Figure 12(b). The fracture features shown in Figures 12(c) and (d) were for the first initiation site, where the crack initiated at the top surface in the vicinity of the TMAZ, while the fracture features shown in Figures 12(e) through (i) were for the second initiation site, which occurred in the NZ (where the SEM images were rotated counterclockwise 90 deg with respect to the image shown in Figure 12(b)). Figure 12(f) was a magnified view near initiation site 2, as indicated in the dashed box in Figure 12(e), while Figure 12(g) corresponded to an X-ray mapping of oxygen  $K_{\alpha 1}$  near the crack initiation site. The third crack also initiated in the NZ. The results shown in Figures 11 and 12 corresponded well to the hardness profile across the weld shown in Figure 8, in which the sample welded with 800 rpm and 100 mm/min exhibited two obvious LHZs between the TMAZ and HAZ (Figure 8(a)), and the fatigue fracture occurred along the LHZs accordingly, while the sample welded using 800 rpm and 400 mm/min did not show such obvious LHZs (Figure 8(c)) and the occurrence of fatigue fracture was shifted to the NZ, with a significantly higher stress amplitude (Figure 9(a) and lower plastic strain amplitude (Figure 9(b)) at different total strain amplitudes. These observations suggested that the LCF resistance of the 7075Al-T651 alloy in the welding condition of 800 rpm and 400 mm/min was much higher than that in the welding condition of 800 rpm and 100 mm/min.

## IV. DISCUSSION

### A. Microstructural Characteristics

#### 1. Recrystallization mechanism

During FSW, the material that flows around the tool undergoes intense plastic deformation at elevated temperatures.<sup>[11]</sup> Restoration of aluminum alloys by dynamic recovery and the dynamic recrystallization (DRX) has been well reviewed.<sup>[33]</sup> The DRX results in the generation of fine and equiaxed grains of 0.1 to 12 μm with predominantly high-angle grain boundaries (HAGBs) in the NZ of friction-stir-welded aluminum alloys,<sup>[7]</sup> magnesium alloys,<sup>[34]</sup> and metal matrix composites.<sup>[35]</sup> The usual definition of recrystallization is the formation and migration of the HAGBs driven by the stored energy of deformation.<sup>[36]</sup> The recrystallization is a nucleation and growth process. The growth is accomplished by the migration of the HAGBs.<sup>[37]</sup> It was reported that deformation efficiency for DRX depends on the composition, crystal structure, deformation history, and stacking-fault energy of the alloy.<sup>[38]</sup> The final grain size is generally determined by the ratio of the rate of nucleation to the rate of grain growth of the new grains.<sup>[39]</sup> The proposed recrystallization mechanisms during FSW include continuous DRX (CDRX),<sup>[4]</sup> geometric DRX,<sup>[11]</sup> and discontinuous DRX.<sup>[11,40]</sup>

In the present study, the fine and equiaxed grains 4.6 to 6.7 μm in size in the NZ of the friction-stir-welded

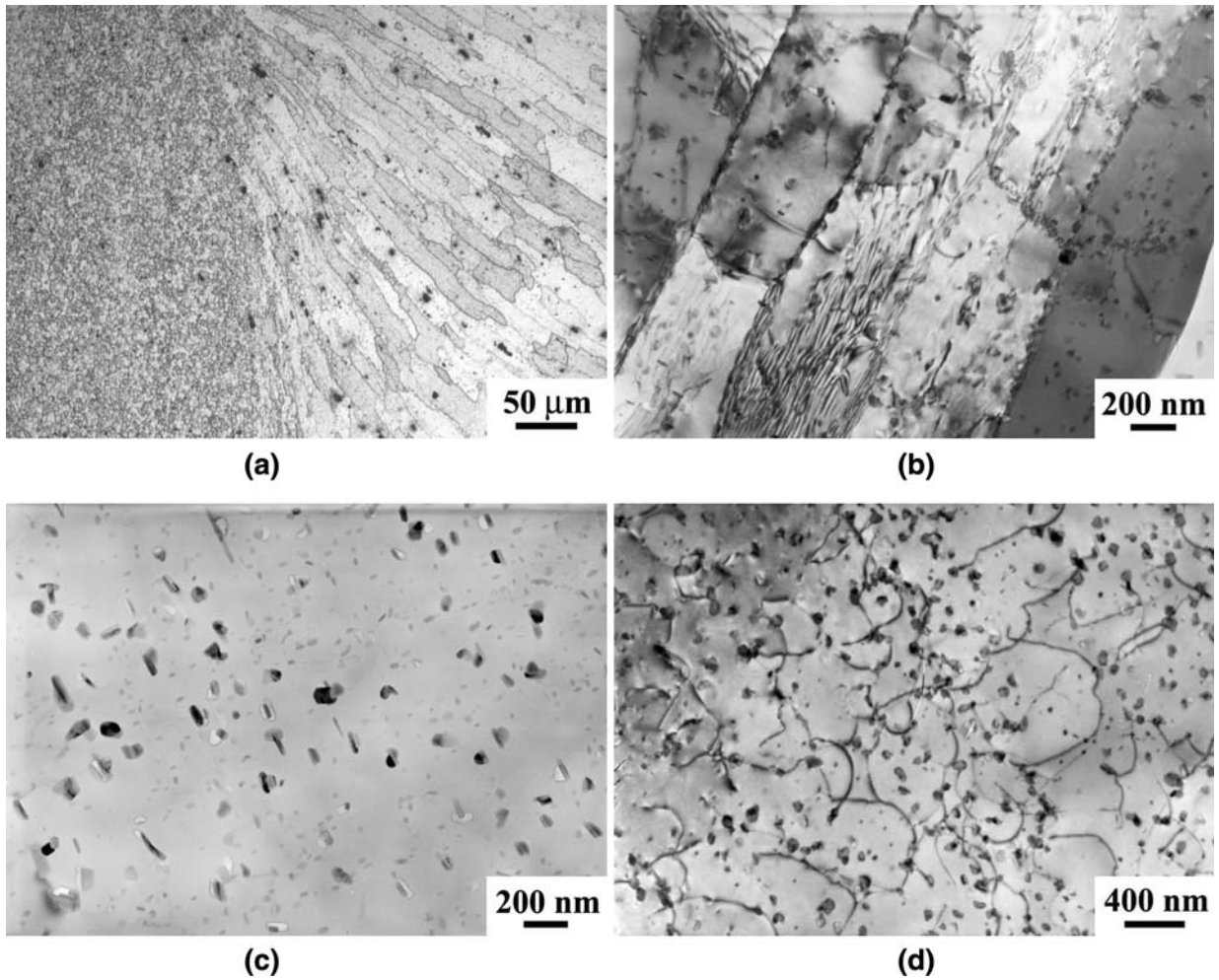


Fig. 7—Microstructure of TMAZ (AS) in friction-stir-welded 7075Al-T651 alloy (800 rpm and 400 mm/min): (a) OM image, deformed grains, (b) TEM image, subgrain structure, (c) TEM image, coarsened precipitates, and (d) TEM image, dislocations pinned by second-phase particles.

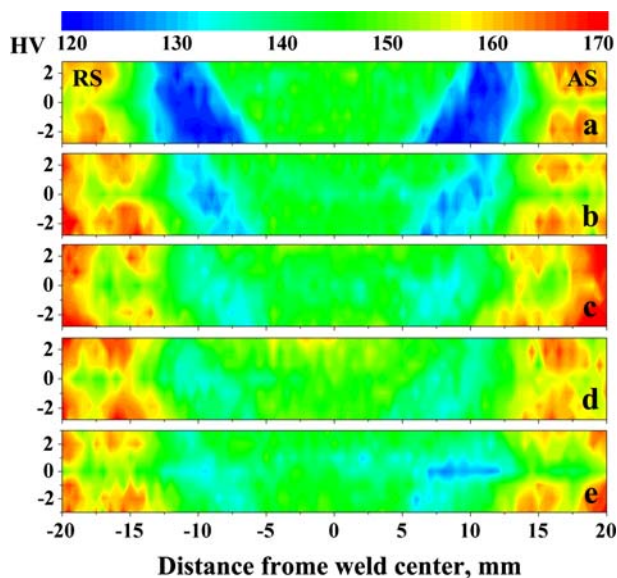
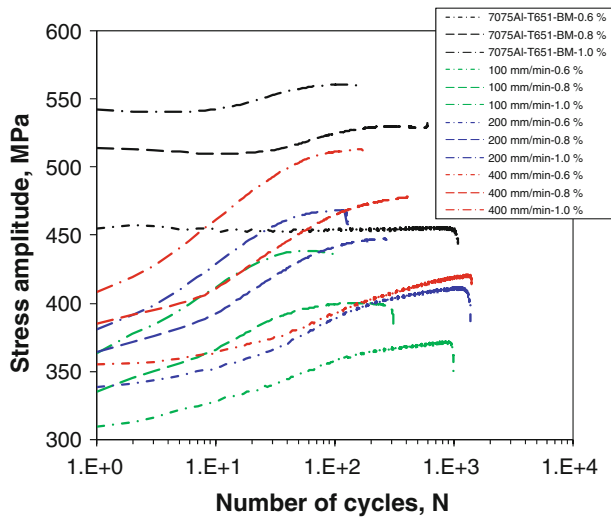


Fig. 8—Microhardness contour maps for the friction-stir-welded 7075Al-T651 joints: (a) 800 rpm and 100 mm/min, (b) 800 rpm and 200 mm/min, (c) 800 rpm and 400 mm/min, (d) 1000 rpm and 400 mm/min, and (e) 1200 rpm and 400 mm/min.

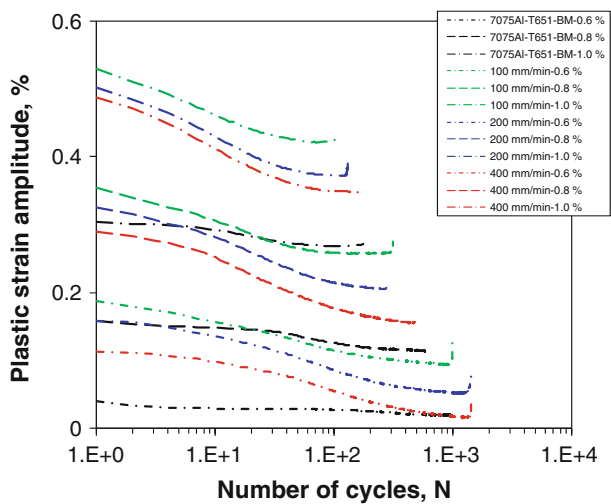
7075Al-T651 alloy were considerably smaller than those in the BM. This indicated that DRX took place in the NZ of the friction-stir-welded 7075Al-T651 alloy. Increasing the welding speed from 100 to 400 mm/min reduced the grain size from 6.7 to 4.6  $\mu\text{m}$ . Rhodes *et al.*<sup>[41]</sup> reported that the initial sizes of newly recrystallized grains in a friction-stir-processed 7075Al alloy were on the order of 25 to 100 nm. These grains then grew to a size equivalent to that observed in friction-stir-processed aluminum alloys, 2 to 5  $\mu\text{m}$ , after heating 1 to 4 minutes at 350  $^{\circ}\text{C}$  (623 K) to 450  $^{\circ}\text{C}$  (723 K).<sup>[41]</sup> Second-phase dispersoids could serve as very effective stabilizers for dislocation substructures and deformation bands.<sup>[42]</sup> Recently, CDRX was proposed as the recrystallization mechanism in friction-stir-welded aluminum alloys.<sup>[4,11,43]</sup> During CDRX, new grains developed *via* a gradual increase in misorientation between subgrains.<sup>[40]</sup> The CDRX modeling in the FSW of AA7075Al-T6 alloy has also been proposed by Buffa *et al.*<sup>[12]</sup>

## 2. Precipitation

Two types of precipitation occur in *C* curves in aluminum alloys.<sup>[44]</sup> One is the precipitation of Cu, Mg, Zn atoms at lower temperatures (20  $^{\circ}\text{C}$  (293 K) to



(a)

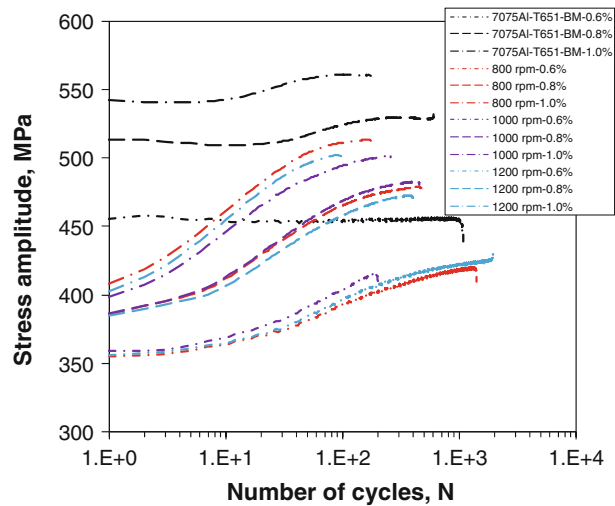


(b)

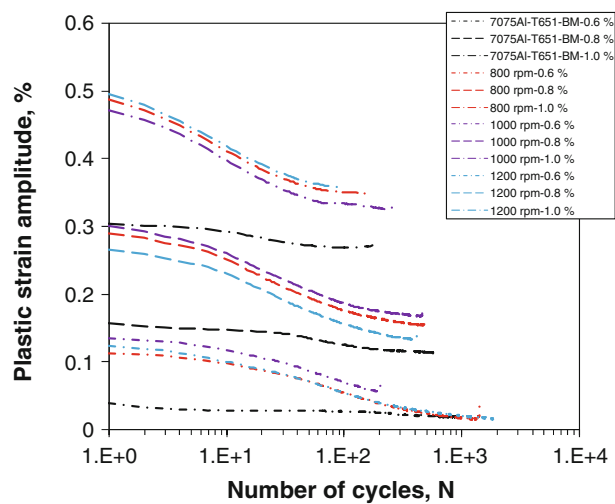
Fig. 9—(a) Stress amplitude and (b) plastic strain amplitude vs the number of cycles at different total strain amplitudes for 7075Al-T651 alloy welded with different welding speeds at a rotational rate of 800 rpm.

400 °C (673 K)), contributing to the age hardening. The other is the precipitation of Zr, Cr, Mn atoms at higher temperatures (350 °C (623 K) to 550 °C (823 K)), contributing to inhibiting grain growth.

The high strength of the 7xxx-series aluminum alloys is due to the fine and uniformly distributed precipitates in the matrix. The usual precipitation sequence of the 7xxx-series aluminum alloys can be summarized as: solid solution → Guinier–Preston (GP) zone → metastable  $\eta'$  ( $\text{Mg}(\text{Zn}, \text{Al}, \text{Cu})_2$ ) → stable  $\eta$  ( $\text{MgZn}_2$ ).<sup>[32]</sup> Two types of GP zones, *i.e.*, solute-rich clusters GP(I) and vacancy-rich solute clusters GP(II), form during the decomposition of the supersaturated solid solution of Al-Zn-Mg alloys.<sup>[4,45]</sup> The GP zones in the 7xxx-series aluminum alloys, as small as 3 nm in diameter, are spherical and coherent.<sup>[39]</sup> The GP zones can serve as nuclei for the



(a)



(b)

Fig. 10—(a) Stress amplitude and (b) plastic strain amplitude vs the number of cycles at different total strain amplitudes for 7075Al-T651 alloy welded with different rotational rates at a welding speed of 400 mm/min.

semicoherent  $\eta'$  phase, or  $\eta'$  can nucleate directly on the dislocations and subgrain boundaries. In the overaged alloys, incoherent  $\eta$  phase grows from the  $\eta'$  particles or nucleates directly on the grain boundaries or other incoherent precipitate-matrix boundaries. Both GP zones and  $\eta'$  are sheared by dislocations.<sup>[39]</sup> The  $\eta'$  is a platelike transition phase (hexagonal), while  $\eta$  is the plate-, lath- or rodlike hexagonal Laves phase.<sup>[46]</sup>

The BM contained three populations of precipitates: intergranular  $\eta$  precipitates on the order of 30 to 40 nm and two sizes of intragranular particles, *i.e.*, 50- to 75-nm dispersoids and 5- to 10-nm high-density fine  $\eta'$  precipitates (Figures 3(c) and (d)). Similar results have also been observed by Mahoney *et al.*<sup>[17]</sup> The DSC analyses indicated the presence of one endothermic peak A at ~188 °C (461 K), which was identified to represent

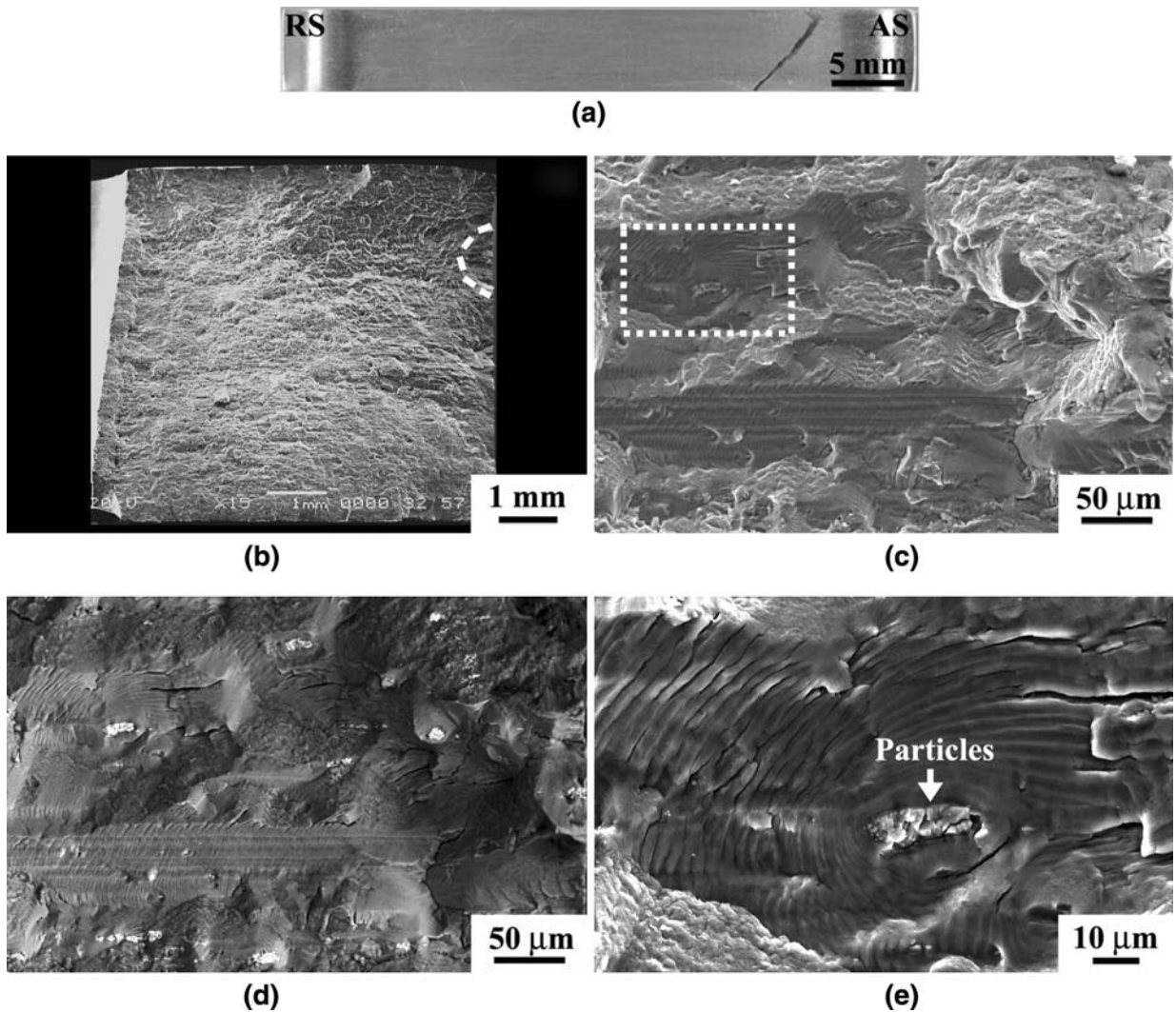


Fig. 11—Typical failure location and SEM micrographs of friction-stir-welded 7075Al-T651 alloy (800 rpm and 100 mm/min) tested at a strain amplitude of 0.6 pct: (a) appearance of a failed friction-stir-welded sample, (b) overall view of the fracture surface at a lower magnification, in which the dashed semicircle indicated the initiation site, (c) secondary electron image, (d) BEI, and (e) fatigue striations and particles at a higher magnification as indicated by dashed box in (c).

the dissolution of  $\eta'$ .<sup>[32]</sup> Based on the DSC results, the  $\eta'$  phase was the main precipitate in the BM. Peak B was associated with the formation of the  $\eta$  phase. Peak C was most likely associated with the formation of the T phase,<sup>[47]</sup> *i.e.*, the dispersoids determined to be  $\text{Mg}_3\text{Cr}_2\text{Al}_{18}$  using XRD and EDS. However, further studies are needed to explain the higher temperature peaks.

The FSW could be considered as a hot-working process. The resulting temperature gradient produced a range of precipitates from the center of the NZ to the BM.<sup>[17]</sup> A solid-state type of phase transformation occurred during cooling of the weld.<sup>[18]</sup> The precipitate distribution was strongly influenced by the thermal hysteresis.<sup>[4,48]</sup> The temperature during FSW was reported to lie between 400 °C (673 K) and 480 °C (753 K) in the 7075 Al alloy, which might be sufficient to force larger precipitates to go fully or partially into solution and reprecipitate in the weld during

cooling.<sup>[4,8,17]</sup> Strengthening precipitates in the NZ went into solution and reprecipitated.

After FSW, the NZ was characterized by a fine and equiaxed recrystallized grain structure. No fine precipitates were observed *via* TEM examinations. Thus, FSW resulted in the dissolution of a fine  $\eta'$  phase. Similar results have also been observed by Mahoney *et al.*<sup>[17]</sup> Dumont *et al.*<sup>[49]</sup> reported that although complete dissolution occurred in the NZ, it recovered some hardness upon cooling and subsequent natural aging. During this period, GP zones nucleated and grew in regions in which supersaturation was sufficient.<sup>[49]</sup> However, Rhodes *et al.*<sup>[8]</sup> reported a high density of randomly oriented intragranular precipitates of  $\text{Mg}_{32}(\text{Al,Zn})_{49}$  with sizes of 60 to 80 nm that have reprecipitated during the FSW process. Charit and Mishra<sup>[14]</sup> reported that there were two main types of particles, *i.e.*, plate-shaped  $\text{MgZn}_2$  precipitates and the chromium-rich spherical  $\text{Mg}_3\text{Cr}_2\text{Al}_{18}$  dispersoids that remained almost unchanged.

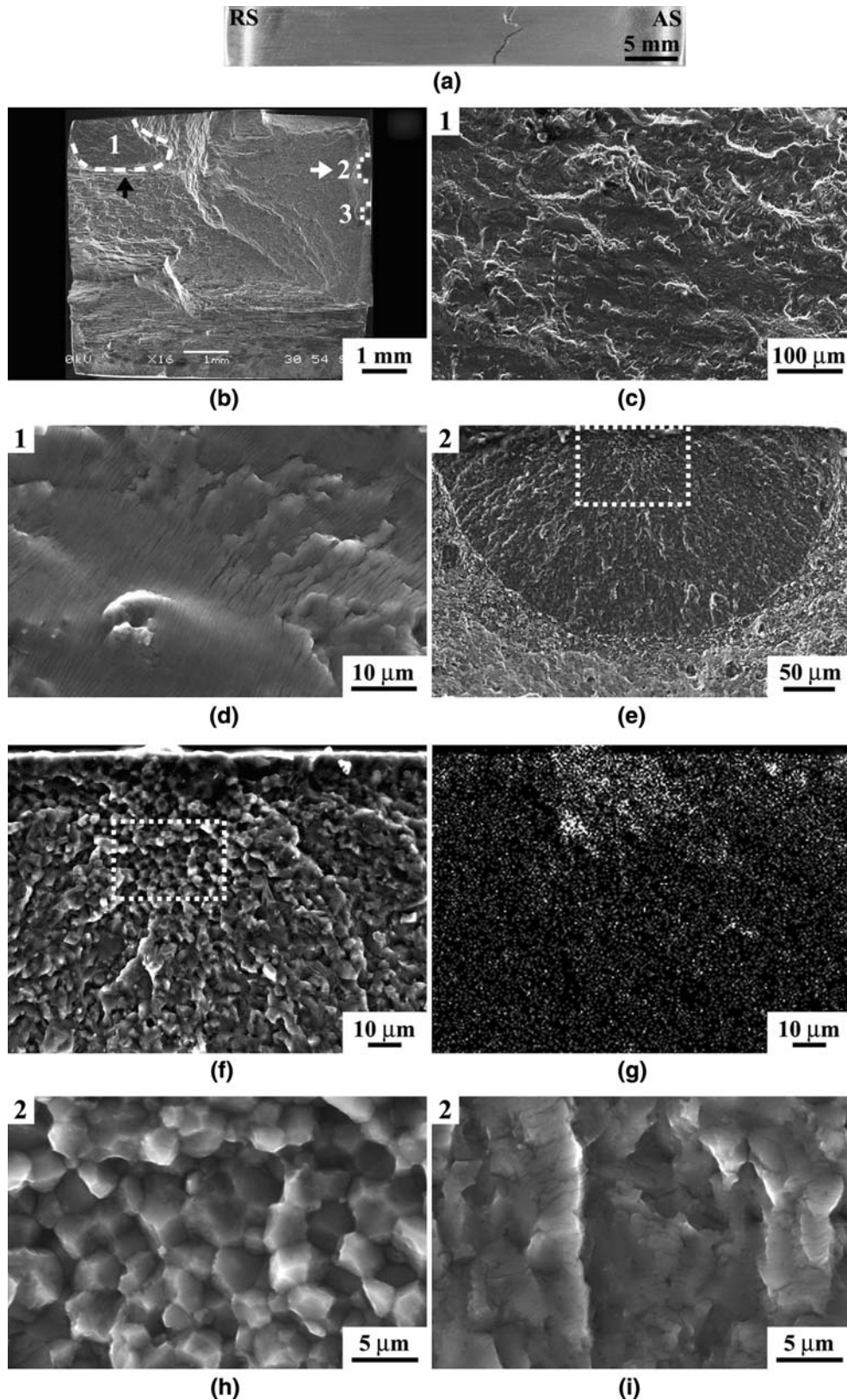


Fig. 12—Typical failure location and SEM micrographs of friction-stir-welded 7075Al-T651 alloy (800 rpm and 400 mm/min) tested at a strain amplitude of 0.6 pct: (a) appearance of a failed friction-stir-welded sample, (b) overall view of the fracture surface with multiple crack initiation sites indicated by three dashed semicircles, (c) magnified view near initiation site No. 1, in (b), (d) fatigue striations at a higher magnification (No. 1), (e) initiation site No. 2, (f) magnified view near initiation site No. 2, (g) EDS mapping of oxygen  $K_{\alpha 1}$  corresponding to (f), (h) further magnified view near initiation site No. 2, as indicated in the dashed box in (f), and (i) fatigue propagation area at a higher magnification, where images (e) through (i) were taken with a counterclockwise rotation of 90 deg.

The transients and gradients in the strain, strain rate, and temperature were inherent in the thermomechanical cycles of FSW.<sup>[33]</sup> Therefore, the distribution, size, and types of precipitates were characterized as sharp spatial gradients in the transition from the BM to the center of the NZ.

As shown in Figure 7, most grains in the TMAZ contained a high dislocation density, thereby resulting in the coarsened precipitates. The precipitation process in aluminum alloys was diffusion controlled.<sup>[50]</sup> Dislocations were favorable nucleation sites for precipitates and short-circuit diffusion paths for solutes.<sup>[51]</sup> This resulted in faster and coarser precipitation on dislocations. Moreover, precipitation at structural defects naturally promoted the stable rather than the metastable phases.

In 7xxx-series aluminum alloys, zirconium- or chromium-rich dispersoids formed during solidification and remained stable during subsequent thermal and mechanical treatments.<sup>[52]</sup> Dispersoids, *i.e.*, Al<sub>12</sub>Mg<sub>2</sub>Cr and Mg<sub>3</sub>Cr<sub>2</sub>Al<sub>18</sub> (*E* phase), played an essential role in grain and subgrain pinning.<sup>[3]</sup> The Mg<sub>3</sub>Cr<sub>2</sub>Al<sub>18</sub> dispersoids had three typical morphologies: rodlike, spherical, and transgranular. Based on their morphologies and chemical composition, the dispersoids in Figures 6(b) and (c) were identified to be the *E* phase, in agreement with the findings of Wagner and Shenoy<sup>[53]</sup> and Li *et al.*<sup>[28]</sup>

Generally, secondary particles could either accelerate or retard the recrystallization process, depending on the interparticle spacings.<sup>[52]</sup> The effect of a secondary particle system upon the recrystallization process was twofold.<sup>[52]</sup> First, it altered the mode of deformation of the alloy. Second, it had a pinning effect on low- and high-angle grain boundaries and on the deformed structure, as presented in Figure 7(d). A detailed analysis of the influence of particle coarsening and dissolution on abnormal grain growth (AGG) has been done by Humphreys.<sup>[54]</sup> The AGG was possible when the pinning parameter, *Z*, is  $0.25 < Z < 1$  ( $Z = 3F_v R/d$ , where  $F_v$  is the volume fraction of particles,  $R$  is the average grain radius, and  $d$  is the average particle diameter).<sup>[54]</sup> The presence of the *E* particles significantly stabilized the grain structure and improved the strength, ductility, fatigue limit, *etc.* The relationship between the Al<sub>3</sub>Zr dispersoids and the stability of the NZ grain structures in the friction-stir-welded AA7010-T7651 alloy has been well studied in detail.<sup>[55]</sup>

### B. Microhardness Profile

It was reported that the hardness profile of friction-stir-welded heat-treatable aluminum alloys greatly depended on the precipitate distribution and only slightly on the grain and dislocation structures.<sup>[56]</sup> In the precipitation-hardened aluminum alloys, FSW resulted in a softened region in the HAZ, which was basically characterized by the dissolution/coarsening of precipitates during the FSW thermal cycle.<sup>[48]</sup> It was also reported that the tensile fracture path of the welds corresponded to the LHZs.<sup>[57,58]</sup> The temperatures during FSW were sufficiently high and the times at the high temperatures were sufficiently long to influence the strengthening precipitates' morphologies. The local

nucleation, growth, and coarsening processes for strengthening precipitates were a function of the temperature, which in turn was a function of distance from the center of the NZ.<sup>[17]</sup> The precipitate distribution was strongly influenced by the thermal hysteresis.<sup>[48]</sup>

The temperature in the NZ during FSW was above the solution temperature of 7xxx-series aluminum alloys; therefore, the  $\eta'$ -strengthening precipitates dissolved into the matrix. The dissolution of the strengthening precipitates resulted in a significantly lower strength and hardness.<sup>[19]</sup> As shown in Figure 8, two issues were worth noting. First, two LHZs were obviously observed due to precipitate overaging,<sup>[57]</sup> crystallographic texture,<sup>[59,60]</sup> and grain/subgrain structure.<sup>[60]</sup> The width of the LHZs increased with decreasing welding speed from 400 to 100 mm/min. The asymmetry of the weld could be noticeable between the AS and the RS. The LHZs between the TMAZ and the HAZ have also been reported in the friction-stir-welded 6061Al-T651 alloy<sup>[58]</sup> and the friction-stir-welded 2519Al-T87 alloy.<sup>[60]</sup> Second, the hardness profile greatly depended on the precipitate distribution and only slightly on the grain size (Figure 5), as was also observed in Reference 48.

### C. Cyclic Hardening Behavior

Higher total strain amplitudes led to a higher degree of cyclic hardening, as seen in Figures 9 and 10. Whether a certain material cyclically hardens or softens depended mainly on the initial condition of the material and, in some cases, also on the magnitudes of the imposed cyclic loads.<sup>[61]</sup>

It is of interest to note that for each curve of the friction-stir-welded joints, the cyclic hardening within the initial 10 to 20 cycles was relatively weak; it then increased quickly as cyclic deformation proceeded (Figures 9 and 10). Afterward, the cycled material exhibited a steady-state characteristic. It was obvious that there were two stages of slopes in the stress amplitude or plastic strain amplitude *vs* the number of cycles. The following relationship was thus proposed to describe the change:<sup>[62]</sup>

$$\frac{\Delta \epsilon_p}{2} = \alpha + \beta \log(N) \quad [1]$$

where  $N$  is the number of cycles,  $\alpha$  is the initial plastic strain amplitude corresponding to approximately the twentieth cycle seen from Figures 9 and 10, and  $\beta$  is the slope, which could be considered as a hardening coefficient. Both  $\alpha$  and  $\beta$  are dependent on the applied strain amplitude.

Figure 13 shows the evaluated slope (absolute value) *vs* the total strain amplitude as being from 0.6 to 1.0 pct for the BM and friction-stir-welded 7075Al-T651 joints. With increasing total strain amplitude, both slopes  $\beta_1$  and  $\beta_2$  increased. The  $\beta_2$  in stage 2 was obviously larger than that of the corresponding  $\beta_1$  in stage 1. The slopes  $\beta_1$  and  $\beta_2$  of the friction-stir-welded 7075Al-T651 joints were larger than those of the BM, indicating the stronger cyclic-hardening character after FSW.

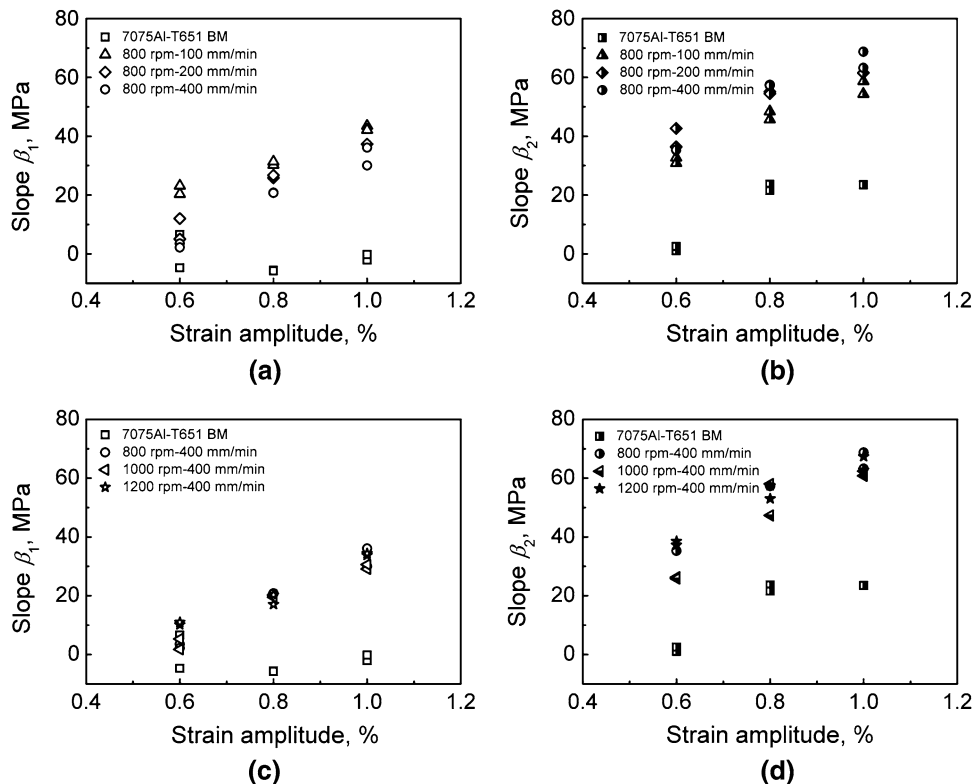


Fig. 13—Slope in Eq. [1] vs strain amplitude: (a)  $\beta_1$ , 800 rpm, (b)  $\beta_2$ , 800 rpm, (c)  $\beta_1$ , 400 mm/min, and (d)  $\beta_2$ , 400 mm/min.

A few typical hysteresis loops at a total strain amplitude of 1.0 pct are shown in Figure 14(a). It is seen that the stress amplitude increased as cyclic deformation progressed, indicating the occurrence of cyclic hardening. Figure 14(b) shows the effect of total strain amplitudes on the shape of hysteresis loops at the midlife cycle. The hysteresis loop widened and its enclosed area increased with increasing strain amplitude.

Energy was dissipated in fatigue because of plastic deformation. The hysteresis loop area, *i.e.*, energy per cycle, was equal to the deformation work produced during one loading cycle. This deformation work was mainly transformed into heat energy and a very small part of it into stored energy. The total hysteresis energy was then equal to the sum of areas of all hysteresis loops, which was sometimes called the fatigue toughness.<sup>[61]</sup> Hysteresis energy provided a useful basis for the establishment of failure criteria in fatigue.<sup>[61]</sup> Based on the recorded loop data, the energy per cycle was evaluated, as shown in Figure 14(c) and Table I. It is seen that the energy per cycle decreased with a decreasing total strain amplitude and with an increasing number of cycles. This represented another way of characterizing the occurrence of cyclic hardening during cyclic deformation.

#### D. Fatigue Crack Initiation and Propagation

The fatigue process can be divided into three stages: crack initiation, crack propagation, and final fast fracture. Fatigue cracks often initiate at the surface or

at voids or second-phase inclusions that serve as stress risers.<sup>[39]</sup> In this study, fatigue cracks initiated from the specimen surface in the friction-stir-welded sample (Figures 11 and 12). The fatigue failure of friction-stir-welded joints has also been observed to initiate at surface roughness or flash on the surface of the joint, as well as at typical FSW defects.<sup>[24]</sup> The factors affecting fatigue crack initiation include the surface finish, grain size, residual stress, environment, frequency of stress cycle, and temperature.<sup>[39]</sup> Commercial metallic alloys are always multiphase materials. Second-phase particles are deliberately introduced to refine the grain size, increase the strength, or simply remain as impurities.<sup>[63]</sup> The role of the particles in the mechanisms of cyclic deformation depends on whether they can be sheared by dislocations.<sup>[63]</sup> Fatigue failure of metallic materials is induced by the nucleation of one or several microcracks that propagate slowly during cyclic loading until one of them reaches the critical size and catastrophic failure occurs.<sup>[63]</sup> Fatigue crack propagation was basically characterized by fatigue striations, together with some secondary cracks, observed at higher magnifications (Figure 11(e)).

As shown in Figure 8, the LHZs became more obvious with a decreasing welding speed from 400 to 100 mm/min (Figures 8(c) to (b) to (d)) while keeping a constant rotational rate of 800 rpm. The samples friction stir welded with 800 rpm and 100 mm/min tended to fail along the LHZs, especially at higher strain amplitudes, *e.g.*, at 0.6 pct (Figure 11). However, for the samples friction stir welded with 800 rpm and 400 mm/min, there were no obvious LHZs (Figure 8(c)).

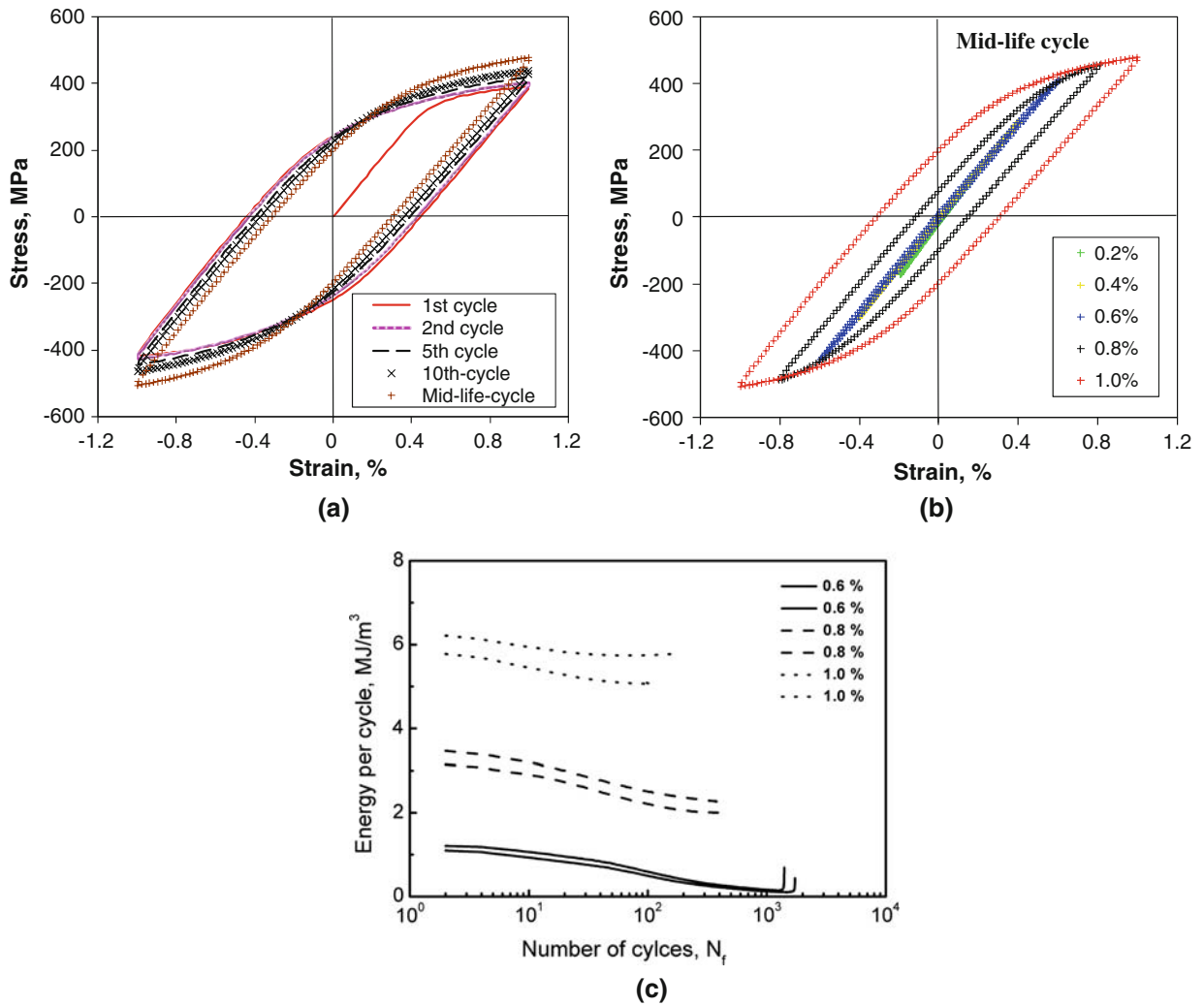


Fig. 14—(a) Hysteresis loop evolution at a given strain amplitude of 1.0 pct, (b) midlife hysteresis loops at different strain amplitudes, and (c) energy per cycle vs the number of cycles for friction-stir-welded 7075Al-T651 alloy at different strain amplitudes (800 rpm and 400 mm/min).

**Table I. Summary of Energy Dissipated during Cyclic Deformation for Friction-Stir-Welded 7075Al-T651 Alloy (800 rpm and 400 mm/min)**

Total Strain Amplitude (%)	Total Energy (MJ/m <sup>3</sup> )	Average Energy per Cycle (MJ/m <sup>3</sup> )	Min. Energy (MJ/m <sup>3</sup> )	Cycle Number Corresponding to the Min. Energy	Total Number of Cycles to Failure ( $N_f$ )	Remaining Cycles After the Min. Energy
0.6	299.0	0.20	0.10	1465	1736	271
0.6	338.8	0.27	0.14	1215	1406	191
0.8	735.5	2.45	2.24	467	478	11
0.8	600.9	2.18	1.95	463	469	6
1.0	504.4	5.80	5.74	58	173	115
1.0	420.8	5.19	5.07	94	107	13

Thus there was no longer fracture along the LHZs and, in this case, the fatigue failure occurred basically in the NZ (Figure 12(a)). The fracture exhibited multiple crack initiations (Figure 12(b)) and the initiation sites demonstrated intergranular cracking or decohesion along the weak grain boundaries of equiaxed grains

(Figures 12(e), (f), and (h)). As revealed by the EDS mapping shown in Figure 12(g), corresponding to Figure 12(f), the oxygen-enrichment zone was seen clearly at the initiation site. The preliminary result would suggest that the intergranular cracking in the NZ was caused by the oxygen-related issues during FSW,

while the intergranular decohesion was normally observed to occur in the stress-corrosion cracking in 7xxx-series aluminum alloys.<sup>[64]</sup> Krupp *et al.*<sup>[65]</sup> also reported the oxygen-induced intergranular fracture in a nickel-base alloy IN718 during mechanical loading at high temperatures. Further studies of this aspect are needed. While the crack initiation was associated with the intergranular decohesion/cracking in the NZ, the crack propagation was characterized by the characteristic fatigue striations (Figures 12(d) and (i)). The fatigue striations normally occurred by a repeated plastic blunting-sharpening process due to the slip of dislocations in the plastic zone at the fatigue crack tip.<sup>[66]</sup>

## V. CONCLUSIONS

1. The FSW resulted in remarkable grain refinement, which was characterized by a fine and equiaxed recrystallized grain structure. The average grain size decreased with an increasing welding speed from 100 to 400 mm/min, but changed less considerably with an increasing rotational rate from 800 to 1200 rpm.
2. While the dissolution of  $\eta'$  ( $\text{Mg}(\text{Zn}, \text{Al}, \text{Cu})_2$ ) precipitates occurred in the NZ, the  $E$ -phase  $\text{Mg}_3\text{Cr}_2\text{Al}_{18}$  dispersoids remained almost unchanged after FSW. Most grains in the TMAZ contained a high density of dislocations with a network subgrain structure due to severe deformation, coupled with coarsened precipitates either within the grain or at the subgrain boundaries. Some dislocations were pinned by  $\text{Mg}_3\text{Cr}_2\text{Al}_{18}$  dispersoids, displaying a characteristic Orowan mechanism of dislocation bowing between the dispersoids.
3. Two LHZs between the TMAZ and HAZ were observed, and their width decreased with increasing welding speed from 100 to 400 mm/min.
4. During cyclic deformation, the friction-stir-welded 7075Al-T651 joints exhibited very strong cyclic hardening behavior with a two-stage character. While the stress amplitude of the friction-stir-welded joints was lower than that of the BM, the cyclic hardening of the friction-stir-welded joints, which increased with increasing strain amplitude, was much stronger than that of the BM.
5. While the stress amplitude of the friction-stir-welded joints increased and the plastic strain amplitude decreased with increasing welding speed, the rotational rate between 800 and 1200 rpm exhibited a less significant effect on the cyclic deformation character.
6. Fatigue failure was observed to occur in the LHZs at a low welding speed of 100 mm/min and in the NZ at a high welding speed of 400 mm/min. Fractography revealed that fatigue cracks initiated from the specimen surface or near-surface defects in the friction-stir-welded joints. When the fatigue failure occurred in the NZ, the initiation site exhibited characteristic intergranular cracking. Crack propagation was characterized by typical fatigue striations, together with some secondary cracks.

## ACKNOWLEDGMENTS

The authors thank the Natural Sciences and Engineering Research Council of Canada (NSERC) (Ottawa, ON, Canada), the Premier's Research Excellence Award (PREA) (Toronto, ON, Canada) of the University of Ottawa (Ottawa, ON, Canada), the Canada Foundation for Innovation (CFI) (Ottawa, ON, Canada), the Ryerson Research Chair (RRC) program of Ryerson University (Toronto, ON, Canada), the National Outstanding Young Scientist Foundation (Grant No. 50525103), National Natural Science Foundation of China, Beijing, China, and the Hundred Talents Program of the Chinese Academy of Sciences (Beijing China) for providing financial support for this collaborative project. The authors also thank Messrs. Q. Li, A. Machin, J. Amankrah, D. Ostrom, and R. Churaman (Ryerson University, Toronto, ON, Canada) for their assistance in the experiments.

## REFERENCES

1. J.R. Davis: *ASM Specialty Handbook, Aluminum and Aluminum Alloys*, The Materials Information Society, Materials Park, OH, 1993.
2. N.U. Deshpande, A.M. Gokhale, D.K. Denzer, and J. Liu: *Metall. Mater. Trans. A*, 1998, vol. 29A, pp. 1191–1201.
3. A. Raghavan, J.Y. Koo, J.W. Steeds, and B.K. Park: *Metall. Trans. A*, 1985, vol. 16A, pp. 1925–36.
4. J.Q. Su, T.W. Nelson, R. Mishra, and M. Mahoney: *Acta Mater.*, 2003, vol. 51, pp. 713–29.
5. M.J. Starink and S.C. Wang: *Acta Mater.*, 2003, vol. 51, pp. 5131–50.
6. W.M. Thomas, E.D. Nicholas, J.C. Needham, M.G. Murch, P. Templesmith, and C.J. Dawes: Great Britain Patent Application 9125978.8, Dec. 1991.
7. R.S. Mishra and Z.Y. Ma: *Mater. Sci. Eng., R*, 2005, vol. R50, pp. 1–78.
8. C.G. Rhodes, M.W. Mahoney, W.H. Bingel, R.A. Spurling, and C.C. Bampton: *Scripta Mater.*, 1997, vol. 36, pp. 69–75.
9. N. Kamp, A. Sullivan, R. Tomasi, and J.D. Robson: *Acta Mater.*, 2006, vol. 54, pp. 2003–14.
10. A. Sullivan and J.D. Robson: *Mater. Sci. Eng., A*, 2008, vol. 478A, pp. 351–60.
11. J.Q. Su, T.W. Nelson, and C.J. Sterling: *Mater. Sci. Eng., A*, 2005, vol. 405A, pp. 277–86.
12. G. Buffa, L. Fratini, and R. Shivpuri: *J. Mater. Process. Technol.*, 2007, vol. 191, pp. 356–59.
13. Z.Y. Ma, R.S. Mishra, and M.W. Mahoney: *Acta Mater.*, 2002, vol. 50, pp. 4419–30.
14. I. Charit, R.S. Mishra, and M.W. Mahoney: *Scripta Mater.*, 2002, vol. 47, pp. 631–36.
15. L. Fratini, G. Buffa, D. Palmeri, J. Hua, and R. Shivpuri: *Sci. Technol. Weld. Join.*, 2006, vol. 11, pp. 412–21.
16. V.M. Linton and M.I. Ripley: *Acta Mater.*, 2008, vol. 56, pp. 4319–27.
17. M.W. Mahoney, C.G. Rhodes, J.G. Flintoff, R.A. Spurling, and W.H. Bingel: *Metall. Mater. Trans. A*, 1998, vol. 29A, pp. 1955–64.
18. K.V. Jata, K.K. Sankaran, and J.J. Ruschau: *Metall. Mater. Trans. A*, 2000, vol. 31A, pp. 2181–92.
19. P.S. Pao, S.J. Gill, C.R. Feng, and K.K. Sankaran: *Scripta Mater.*, 2001, vol. 45, pp. 605–12.
20. M. Ericsson and R. Sandstrom: *Int. J. Fatigue*, 2003, vol. 25, pp. 1379–87.
21. R. John, K.V. Jata, and K. Sadananda: *Int. J. Fatigue*, 2003, vol. 25, pp. 939–48.
22. M.N. James, D.J. Hughes, D.G. Hattingh, G.R. Bradley, G. Mills, and P.J. Webster: *Fatigue Fract. Eng. Mater. Struct.*, 2004, vol. 27, pp. 187–202.

23. A.P. Reynolds, W. Tang, Z. Khandkar, J.A. Khan, and K. Linder: *Sci. Technol. Weld. Join.*, 2005, vol. 10, pp. 190–99.
24. S. Lomolino, R. Tovo, and J.D. Santos: *Int. J. Fatigue*, 2005, vol. 27, pp. 305–16.
25. P.S. De, R.S. Mishra, and C.B. Smith: *Scripta Mater.*, 2009, vol. 60, pp. 500–03.
26. M.N. James, D.G. Hattingh, and G.R. Bradley: *Int. J. Fatigue*, 2003, vol. 25, pp. 1389–98.
27. M. Hornqvist and B. Karlsson: *Mater. Sci. Eng., A*, 2008, vol. 479A, pp. 345–55.
28. P. Li, N.J. Marchand, and B. Ilchner: *Mater. Sci. Eng., A*, 1989, vol. 119A, pp. 41–50.
29. M. Czechowski: *J. Mater. Process. Technol.*, 2005, vols. 164–165, pp. 1001–06.
30. L. Ceschini, I. Boromei, G. Minak, A. Morri, and F. Tarterini: *Composites Part A*, 2007, vol. 38, pp. 1200–10.
31. L. Ceschini, I. Boromei, G. Minak, A. Morri, and F. Tarterini: *Compos. Sci. Technol.*, 2007, vol. 67, pp. 605–15.
32. C.W. Bartges: *Scripta Metall. Mater.*, 1993, vol. 28, pp. 1039–42.
33. T.R. McNelley, S. Swaminathan, and J.Q. Su: *Scripta Mater.*, 2008, vol. 58, pp. 349–54.
34. A.H. Feng and Z.Y. Ma: *Acta Mater.*, 2009, vol. 57, pp. 4248–60.
35. A.H. Feng, B.L. Xiao, and Z.Y. Ma: *Mater. Sci. Eng., A*, 2008, vol. 497A, pp. 515–18.
36. C.W. Su, L. Lu, and M.O. Lai: *Philos. Mag.*, 2008, vol. 88, pp. 181–200.
37. J.G. Byrne: *Recovery, Recrystallization, and Grain Growth*, The Macmillan Company, New York, NY, 1965, pp. 60–92.
38. B.C. Ko and Y.C. Yoo: *J. Mater. Sci.*, 2000, vol. 35, pp. 4073–77.
39. A.M. Russell and K.L. Lee: *Structure-Property Relations in Nonferrous Metals*, John Wiley & Sons, Inc., New York, NY, 2005, pp. 69–75.
40. J.Q. Su, T.W. Nelson, and C.J. Sterling: *Philos. Mag.*, 2006, vol. 86, pp. 1–24.
41. C.G. Rhodes, M.W. Mahoney, W.H. Bingel, and M. Calabrese: *Scripta Mater.*, 2003, vol. 48, pp. 1451–55.
42. R. Kaibyshev, O. Sitdikov, A. Goloborodko, and T. Sakai: *Mater. Sci. Eng., A*, 2003, vol. 344A, pp. 348–56.
43. K.V. Jata and S.L. Semiatin: *Scripta Mater.*, 2000, vol. 43, pp. 743–49.
44. H. Yoshida: *Mater. Sci. Forum*, 1996, vols. 204–206, pp. 657–66.
45. L.K. Berg, J. Gjønnes, V. Hansen, X.Z. Li, M.K. Wedel, G. Waterloo, D. Schryvers, and L.R. Wallenberg: *Acta Mater.*, 2001, vol. 49, pp. 3443–51.
46. R.M. Allen and J.B.V. Sande: *Acta Metall.*, 1980, vol. 28, pp. 1185–95.
47. J. Buha, R.N. Lumley, and A.G. Crosky: *Mater. Sci. Eng., A*, 2008, vol. 492A, pp. 1–10.
48. Y.S. Sato, H. Kokawa, M. Enomoto, and S. Jogan: *Metall. Mater. Trans. A*, 1999, vol. 30A, pp. 2429–37.
49. M. Dumont, A. Steuwer, A. Deschamps, M. Peel, and P.J. Withers: *Acta Mater.*, 2006, vol. 54, pp. 4793–4801.
50. R.S. Yassar, D.P. Field, and H. Weiland: *Metall. Mater. Trans. A*, 2005, vol. 36A, pp. 2059–65.
51. I. Dutta and D.L. Bourell: *Acta Metall. Mater.*, 1990, vol. 38, pp. 2041–49.
52. N. Ryum: *Acta Metall.*, 1969, vol. 17, pp. 269–78.
53. J.A. Wagner and R.N. Shenoy: *Metall. Trans. A*, 1991, vol. 22A, pp. 2809–18.
54. F.J. Humphreys: *Proceedings of the Grain Growth in Polycrystalline Materials III*, H. Weiland, B.L. Adams, and A.D. Rollett, eds., TMS, Warrendale, PA, 1998, p. 13.
55. K.A.A. Hassan, A.F. Norman, D.A. Price, and P.B. Prangnell: *Acta Mater.*, 2003, vol. 51, pp. 1923–36.
56. C. Genevois, A. Deschamps, A. Denquin, and B.D. Cottignies: *Acta Mater.*, 2005, vol. 53, pp. 2447–58.
57. F.C. Liu and Z.Y. Ma: *Metall. Mater. Trans. A*, 2008, vol. 39A, pp. 2378–88.
58. A.H. Feng, D.L. Chen, and Z.Y. Ma: *Mater. Sci. Forum*, 2009, vols. 618–619, pp. 41–44.
59. Y.S. Sato and H. Kokawa: *Metall. Mater. Trans. A*, 2001, vol. 32A, pp. 3023–31.
60. R.W. Fonda and J.F. Bingert: *Metall. Mater. Trans. A*, 2004, vol. 35A, pp. 1487–99.
61. B.I. Sandor: *Fundamentals of Cyclic Stress and Strain*, The University of Wisconsin Press, Madison, WI, 1972, pp. 54–63.
62. S. Begum, D.L. Chen, S. Xu, and A.A. Luo: *Int. J. Fatigue*, 2009, vol. 31, pp. 726–35.
63. J. Llorca: *Prog. Mater. Sci.*, 2002, vol. 47, pp. 283–353.
64. *ASM Handbook, Formerly Ninth Edition, Metals Handbook, Volume 12, Fractography*, The Materials Information Society, 2007, pp. 35.
65. U. Krupp, W. Kane, J.A. Pfaendtner, D.Y. Liu, C. Laird, and C.J. McMahon, Jr.: *Mater. Res.*, 2004, vol. 7, pp. 35–41.
66. C. Laird: *Fatigue Crack Propagation*, ASTM STP 415, ASTM, Philadelphia, PA, 1967, pp. 131–68.